Available online at www.sciencedirect.com
ScienceDirect
Geochimica et Cosmochimica Acta 73 (2009) 239–255
Geochimica et Cosmochimica Acta
www.elsevier.com/locate/gca

Trace element partitioning between carbonatitic melts and mantle transition zone minerals: Implications for the source of carbonatites

Célia Dalou [a,*], Kenneth T. Koga [a], Tahar Hammouda [a], Franck Poitrasson [b]

[a] Laboratoire Magmas et Volcans, UMR 6524, Université Blaise Pascal Clermont-Ferrand, France
[b] Laboratoire d'étude des Mécanismes et Transferts en Géologie, Centre National de la Recherche Scientifique—Université de Toulouse—IRD, 14-16, avenue E. Belin, 31400, Toulouse, France

Received 14 March 2008; accepted in revised form 12 September 2008; available online 30 September 2008

Abstract

The occurrence of CO_2-rich lavas (carbonatites, kimberlites) and carbonate-rich xenoliths provide evidence for the existence of carbonatitic melts in the mantle. To model the chemical composition of such melts in the deep mantle, we experimentally determined partition coefficients for 23 trace elements (including REE, U-Th, HFSE, LILE) between deep mantle minerals and carbonatite liquids at 20 and 25 GPa and 1600 °C. Under these conditions, majoritic garnet and $CaSiO_3$ perovskite are the main reservoirs for trace elements. This study used both femtosecond LA-ICP-MS and SIMS techniques to measure reliable trace element concentrations. Comparison of the two techniques shows a general agreement, except for Sc and Ba. Our experimentally determined partition coefficients are consistent with the lattice strain model. The data suggest an effect of melt structure on partition coefficients in this pressure range. For instance, strain-free partition coefficient (D_0) for majorite–carbonatite melts do not follow the order of cation valence, $D_0^{2+} > D_0^{3+} > D_0^{4+}$, observed for majorite–$CO_2$-free silicate melts. The newly determined partition coefficients were combined with trace element composition of majoritic garnets found as inclusions in diamond to model trace element patterns of deep-seated carbonatites. The result compares favorably with natural carbonatites. This suggests that carbonatites can originate from the mantle transition zone.

1. INTRODUCTION

Degassing of CO_2 from mid-ocean ridge basalts (Javoy and Pineau, 1991; Sarda and Guillot, 2005), CO_2-rich lavas like kimberlites (Price et al., 2000) and carbonatites (Krafft and Keller, 1989; Keller and Krafft, 1990) attest to the presence of CO_2 in the Earth's mantle. As CO_2 mass-balance demonstrates, only 20–40% of the subducted CO_2 is degassed by volcanoes (Zhang and Zindler, 1993; Coltice et al., 2004). These observations require the existence of a deep carbon reservoir in the mantle. Furthermore, experimental studies indicate that CO_2 forms stable phases at various depths (including great depths) during subduction processes (Molina and Poli, 2000; Hammouda, 2003; Dasgupta et al., 2004) and that CO_2 in the deep mantle likely induces the formation of carbonatitic melts (Wyllie and Huang, 1975; Eggler, 1976; Green and Wallace, 1988).

Carbonatitic melts are considered as effective metasomatic agents because of their excellent wetting properties (Hunter and McKenzies, 1989; Watson et al., 1990), high migration rates (Hammouda and Laporte, 2000) and characteristic chemical signature (Green and Wallace, 1988; Jones, 1989; Meens et al., 1989). For example, rare earth element (REE) enrichment and high field strength element (HFSE) depletion in oceanic and continental xenoliths are often attributed to carbonatitic metasomatism (e.g. Menzies and Wass, 1983; O'Reilly and Griffin, 1988; Yaxley et al., 1991; Dupuis et al., 1992; Hauri et al., 1993; Ionov

* Corresponding author. Fax: +33 4 73 34 67 44.
E-mail address: c.dalou@opgc.univ-bpclermont.fr (C. Dalou).

0016-7037/$ - see front matter © 2008 Elsevier Ltd. All rights reserved.
doi:10.1016/j.gca.2008.09.020

et al., 1993; Rudnick et al., 1993; Ionov, 2001). Furthermore, the inferred presence of high-pressure mineral inclusions in diamond (Harte et al., 1999; Hutchison et al., 2001; Kunz et al., 2002) suggests the existence of carbon-bearing fluids at pressures corresponding to depths of 600 km or more. Chemical interactions between carbonatitic melts and upper mantle minerals have previously been modeled using trace element partition coefficients collected between 2 and 6 GPa (Sweeney et al., 1992; Klemme et al., 1995; Blundy and Dalton, 2000; Adam and Green, 2001; Keshav et al., 2005). However, element partitioning at higher pressures for example at the conditions of the transition zone, is still unknown. Here we present new major and trace element partitioning data between majoritic garnet, $CaSiO_3$ perovskite and carbonatitic melts at conditions of the lowermost transition zone and uppermost lower mantle. To emphasize the specific nature of carbonatitic and silicate metasomatism, we compare our new partitioning data with previous studies obtained in CO_2-free compositions (Corgne and Wood, 2004; Walter et al., 2004; Corgne et al., 2005).

2. MATERIALS AND METHODS

2.1. Experimental procedure

The starting material was prepared by mixing 79.8 wt% of a pyrolite composition (Green and Ringwood, 1963; Table 1) with 20.2 wt% of a natural dolomite. This composition was chosen to achieve liquidus saturation of mantle phases with sufficiently large quantity of liquid. The pyrolite powder was prepared from a synthetic gel that was annealed for 40 min at 1400 °C in a 1 atm gas-mixing furnace, at about 2 log units above the iron–wüstite oxygen buffer (Table 1). The natural dolomite (from Ben Gasseur, Tunisia) was chosen because its major element composition is close to that calculated for a dolomite in equilibrium with the deep mantle. This dolomite was crushed and sieved, and from the 400 μm fraction clean dolomite grains were handpicked under a binocular microscope. After grinding to μm-size grains, the dolomite and pyrolite powders were homogenized under ethanol in an agate mortar. The mixture was doped at the 100–200 ppm concentration level with a suite of trace elements that were added to the powder as a multi-element solution (Table 2). Element concentration in the final mixture was approximately 100 ppm (La, Ce, Nd, Sm, Eu, Gd, Tb, Dy, Ho, Er, Yb, Lu and Sc, Nb, Ta and U) except for Zr, Hf, Ba, Rb and Th, for which doping was 200 ppm. The doped mixture was stored in a drying oven at 150 °C. Although the starting powder was kept dry, the final mixture retained approximately 1500 ppm H_2O by weight, determined by the infrared absorption of a compacted powder pellet.

The experiments were performed at conditions ranging from 1500 to 1700 °C and from 10 to 25 GPa using a multi-anvil apparatus (Kawai and Endo, 1970) fitted with a Walker-type module (Walker et al., 1990) at the "Laboratoire Magmas et Volcans" (LMV) in Clermont-Ferrand, France. The starting powder was packed in an Au capsule (1mm outer diameter), which was welded shut by electric arc welding. We have employed a standard sample assembly, which consists of a ceramic octahedron (MgO with 5% Cr_2O_3), a ZrO_2 sleeve used as thermal insulator (except for 7/2.5 assembly), a $LaCrO_3$ stepped or straight furnace (stepped for 14/8 assembly and straight for 10/4 and 7/2.5 assemblies), and a MgO sleeve that isolates the capsule

Table 1
Major and minor element concentrations of starting materials and run products

Oxides (wt%)	SiO_2	TiO_2	Al_2O	Cr_2O_3	FeO	MnO	MgO	CaO	Na_2O	K_2O	CO_2[c]	Total
Starting compositions												
Pyrolite[a]	42.70	0.18	3.14	0.453	7.49	0.14	37.70	2.91	0.41	0.001		95.27
Dolomite [20][b]					14.30(88)	0.38(14)	12.02(58)	28.45(58)	0.03(6)	0.008(20)	44.80(102)	99.99
Mixture	34.10	0.14	2.51	0.36	8.86	0.19	32.53	8.06	0.33	0.002	9.03	96.22
#743 (20 GPa-1600 °C)												
Maj [13]	49.38(145)	0.11(10)	8.56(62)	1.00(12)	6.14(38)	0.18(8)	27.11(135)	6.60(106)	0.05(4)	0.001(10)	0,138	98.30
CaPv[d] [8]	37.29(126)	4.54(24)	2.54(21)	0.35(12)	1.44(52)	0.03(6)	0.74(20)	40.13(89)	0.03(4)	0.006(28)		87.12
P[7]	40.03(94)	0.24(90)	0.45(20)	0.15(6)	7.46(80)	0.10(4)	49.73(252)	0.04(4)	0.04(2)	0.003(3)		98.24
Per [3]	0.16(8)	0.02(4)	0.18(4)	0.39(8)	23.86(100)	0.29(8)	72.22(272)	0.07(2)	0.14(2)	0.000 (0)		97.34
Melt [5]	11.50(20)	0.32(32)	0.10 4)	0.04(8)	4.90(22)	0.25(4)	20.85(118)	27.62(46)	1.43(4)	0.257 (4)	32.72	100.00
#787 (25 GPa-1600 °C)												
Maj [6]	46.73(100)	0.019(29)	14.09(58)	1.48(19)	7.32(27)	0.47(3)	25.05(19)	4.98(30)	0.18(4)	0.007(26)		100.32
CaPv [9]	48.57(99)	0.69(7)	.08(25)	0.07(5)	0.35(39)	0.06(8)	0.10(2)	46.32(95)	0.02(1)	0.003(6)		97.26
MgPv [5]	53.03(187)	0.23(7)	4.37(70)	0.43(11)	9.15(173)	0.12(6)	33.39(134)	0.11(4)	0.008(22)	0.007(11)		100.84
γ [4]	40.34(58)	0.012(48)	0.08(4)	0.15(5)	13.94(15)	0.07(2)	43.91(114)	0.05(5)	0.008(19)	0.009(17)		98.57
Mst [3]	0.18(52)	0.02(3)	0.03(10)	0.04(8)	2.65(65)	0.08(10)	43.16(940)	0.24(27)	0.00(0)	0.01(2)	53.46	100.00
Melt [3]	7.46(114)	0.15(5)	0.63(11)	0.14(1)	8.57(73)	0.45(3)	22.13(25)	16.21(402)	0.71(9)	0.13(1)	43.42	100.00

Number in parentheses represents two standard deviations (2σ) in terms of least significant digits. Maj, majorite garnet; β, wadsleyite; γ, ringwoodite; CaPv, $CaSiO_3$ perovskite; MgPv, $MgSiO_3$ perovskite; Per, periclase; Mst, magnesite; Melt, quenched carbonate melt.

[a] Analysed by ICP-AES.

[b] Numbers of electron microprobe analyses given in square brackets.

[c] CO_2 was calculated by difference.

Table 2
Trace element concentrations (in ppm) of starting material and run product #743 (20 GPa, 1600 °C)

Starting doped powder		Majorite		Melt		$D_{Maj/Melt}$			CaPv	PvCaPv/Melt
		LA-ICP-MS [3][a]	SIMS [4]	LA-ICP-MS [2]	SIMS [3]	LA-ICP-MS	SIMS	Preferred[c]	SIMS [I]	
Sc	97	33(5)	54(6)	5.78(6)	19.3(6)	5.71(90)	2.8(7)	—	27.0(5)	1.40(7)
Rb	103	n.m.	6.4(6)	n.m.	1151(64)	—	0.0055(14)	0.0055(14)	15.11(9)	0.013(1)
Sr	102	1.9(2)	2.8(4)	637(14)	636(20)	0.0030(4)	0.0044(12)	0.0031(12)	279(5)	0.44(2)
Y	104	242(7)	279(29)	123(2)	109(10)	1.97(9)	2.57(78)	1.98(78)	3320(15)	30(3)
Zr	194	557(46)	733(173)	747(18)	546(42)	0.75(8)	1.34(74)	0.75(74)	2098(25)	3.8(3)
Nb	74	3.4(10)	4.6(14)	558(10)	412(49)	0.006(2)	0.01(1)	0.007(10)	361(7)	0.88(12)
Ba	187	0.43(4)	0.16(10)	1154(23)	1221(137)	0.00038(4)	0.0001(2)	0.0001(2)*	5.5(7)	0.005(1)
Lc[b]	*82*	*12.2(88)*	*12.0(55)*	*3981(55)*	*4050(81)*	*0.0031(23)*	*0.0003(1)*	0.003(2)	24900(89)	6.2(1)
Ce	102	4.4(13)	5.6(19)	288(7)	308(33)	0.015(5)	0.018(8)	0.016(8)	5505(30)	18(2)
Nd	94	n.m.	16(5)	n.m.	258(29)	—	0.061(25)	0.061(25)	6925(79)	27(3)
Sm	94	32(4)	45(16)	142(2)	196(36)	0.22(3)	0.23(12)	0.22(3)	7230(48)	37(7)
Eu	93	45(5)	68(14)	124(0.09)	207(66)	0.37(4)	0.33(17)	0.36(17)	7240(40)	35(11)
Gd	93	66(5)	n.m.	122(0.05)	149(5)	0.54(4)	—	0.54(4)	5235(33)	35(1)
Tb	94	n.m.	142(25)	n.m.	120(17)	—	1.2(4)	0.46(13)	5960(53)	50(7)
Dy	95	n.m.	194(27)	n.m.	126(13)	—	1.5(4)	0.64(13)	4825(59)	38(4)
Ho	91	150(5)	225(30)	82(0.6)	94(8)	1.83(8)	2.4(5)	1.84(2)	3538(27)	38(3)
Er	96	185(5)	260(25)	77(0.04)	88(16)	2.40(6)	2.9(8)	2.4(9)	2877(38)	33(6)
Yb	95	204(2)	315(20)	58(0.6)	74(9)	3.55(7)	4.3(8)	3.6(8)	1900(33)	26(4)
Lu	96	243(13)	353(16)	58(0.3)	64(6)	4.2(3)	5.5(8)	4.3(8)	1535(13)	24(2)
Hf	192	324(38)	n.m.	358(0.07)	236(8)	0.91(11)	—	0.91(11)	1128(24)	4.8(3)
Ta	41	2.7(7)	n.m.	428(0.05)	n.m.	0.006(2)	—	0.006(2)	n.m.	—
Th	189	1.9(13)	3.7(11)	58(0.5)	49(8)	0.034(2)	0.08(6)	0.04(6)	—	—[d]
U	121	2.09(12)	3.5(27)	92(1)	69(17)	0.023(13)	0.05(9)	0.023(90)	6580(60)	95(24)

Number in parentheses represents two standards deviations in terms of least units cited. n.m., not measured. Doped powder was analysed by ICP-MS.

[a] Numbers in square brackets are numbers of LA-ICP-MS and SIMS analyses.

[b] La concentration in melt and mass-balance are suspect (see text). La data are presented because they are consistent with lattice strain models (see below).

[c] Preferred D are weighted mean calculated from D determined by LA-ICP-MS and SIMS, except for * notation, D are chosen for reasons justified in the text.

[d] The concentration analysis is suspect and is not presented.

from the furnace (Hammouda, 2003). All assembly parts except the capsule were fired for 2 h at 1000 °C in a 1 atm furnace immediately before the experiments. During the experiment, temperature was monitored by a $W_{95}Re_5$–$W_{74}Re_{26}$ thermocouple axially placed above the capsule and was controlled by a constant power setting (the uncertainty due to this procedure is estimated to +5/−15 °C), using a Eurotherm 900 controller. The 10 GPa experiments were performed with a 14/8 assembly calibrated against the coesite–stishovite transition (Akaogi et al., 1995) and the Mg_2SiO_4 α–β transition (Morishima et al., 1994). The 15 and 20 GPa experiments were performed with a 10/4 assembly calibrated against the forsterite β–γ transition (Katsura and Ito, 1989; Irifune et al., 1996; Katsura et al., 2003). The 25 GPa experiments were performed with a 7/2.5 assembly calibrated against the ZnS transition (Pan et al., 2002), GaAs transition (Mc Mahon et al., 1998) and GaP transition (Itie et al., 1989). Our high temperature calibration of this assembly is incomplete and we have reported the pressure on the basis of the room temperature calibration. The previous Mg-perovskite forming experiments by LMV group suggest a −5% relative correction to the room temperature calibration curve. After pressurization, the sample was annealed at high temperature for more than 23 h. Before decompression, the power applied to the furnace was shut and the experiments were quenched rapidly (500 °C in the first second of the quench). The recovered capsule was mounted in epoxy resin and polished for microanalyses by electron microprobe, femtosecond laser ablation–inductively coupled plasma–mass spectrometry (LA-ICP-MS) and secondary ion mass spectrometry SIMS.

2.2. Analytical procedure

Major element abundances in the samples were analyzed with a CAMECA SX100 electron microprobe at the LMV. For silicate phases, analytical conditions were 15 kV accelerating voltage and 15 nA beam current and a focused beam was used. For melt and carbonate phases, a 8 nA beam current was selected and a 5 μm defocused beam or a 20 × 20-μm scanning area were employed depending on phase morphology. The calibration standards used in our laboratory, the detail of counting time, choices of spectrometers were described elsewhere (Hammouda, 2003).

Trace element concentrations were determined at the LMTG, Toulouse with an Agilent 7500 quadrupole ICP-MS coupled to a Ti: sapphire femtosecond laser ablation (Pulsar-10, Amplitude Technologies). The laser wavelength was 800 nm with maximum output energy of 12 mJ. Analyses were made with a laser pulse frequency of 5 Hz when each pulse lasts 50–60 fs. Additional details on the LA-ICP-MS techniques used can be found in Freydier et al. (2008). Twenty-two masses were collected with an integration time per mass of 25 ms. The beam diameter was 26 μm. The following masses were analyzed: ^{29}Si, ^{43}Ca, ^{44}Ca, ^{45}Sc, ^{85}Rb, ^{88}Sr, ^{89}Y, ^{90}Zr, ^{93}Nb, ^{137}Ba, ^{139}La, ^{140}Ce, ^{147}Sm, ^{153}Eu, ^{157}Gd, ^{165}Ho, ^{166}Er, ^{172}Yb, ^{175}Lu, ^{178}Hf, ^{181}Ta, ^{232}Th and ^{238}U. Calcium abundance measured on electron microprobe was used as internal standard. A typical signal acquisition started by collecting a background signal for 30 s, and then, depending of crystal size, laser firing lasted from 30 to 80 s. The NIST 610 glass was used as an external standard (Reed, 1992; Pearce et al., 1997). Previous work has shown that matrix-matching calibration is not required for accurate femtosecond LA-ICP-MS analyzes of variety of sample matrix (Poitrasson et al., 2003). The glass BCR-2G (Wilson, 1997) was analyzed also to check analyses accuracy and precision. The maximum detection limit was about 2 ppm for Sc, and it was typically lower by two orders of magnitude for the other elements.

Secondary ionic mass spectrometry analyses were carried out on a Cameca IMS3f (Woods Hole Oceanographic Institution, WHOI, USA) and on a Cameca IMS4f (Laboratoire Géosciences Montpellier, GM, France). A primary O^- ion beam of 6 nA was accelerated to 10 kV before hitting the sample. To reduce mass interference by molecular ion species, the energy filtering method was used where secondary ions were subjected a 4500 V accelerating voltage with a −90 V offset with ±25 eV energy window for WHOI SIMS, and with an −80 V offset with ±30 eV energy window for GM SIMS (Shimizu and Hart, 1982). The primary beam size was set to approximately 20 μm on WHOI SIMS and to 50 μm (Kohler illumination) on GM SIMS. Counting time for each mass was chosen to attain a minimum of 1000 counts per cycle for 500 ppm concentration, and varied from 10 to 30 s. Five to ten cycles of acquisitions were done for each mass. The following masses were analyzed: ^{24}Mg, ^{28}Si (WHOI), ^{30}Si (GM), ^{40}Ca, ^{45}Sc, ^{47}Ti, ^{85}Rb, ^{88}Sr, ^{89}Y, ^{90}Zr, ^{93}Nb, ^{137}Ba (GM), ^{138}Ba (WHOI), ^{139}La, ^{140}Ce, ^{146}Nd, ^{147}Sm, ^{153}Eu, ^{159}Gd (WHOI), ^{160}Gd (GM), ^{163}Dy, ^{165}Ho, ^{166}Er, ^{172}Yb (GM), ^{174}Yb (WHOI), ^{175}Lu, ^{178}Hf, ^{208}Pb (WHOI), ^{232}Th and ^{238}U. The trace element concentrations were determined by taking ratios of each mass over ^{28}Si (WHOI) and ^{30}Si (GM), and the ratio was multiplied by a calibration factor after correcting for isotopic abundances. Concentrations recalculated using ^{40}Ca as the reference mass showed no systematic offset induced by the choice of the reference element. The calibration factor was determined from the measurement of NIST 610 (Reed, 1992; Pearce et al., 1997) at the beginning and the end of each analytical session. Geostandard KL2-G (Jochum and Stoll, 2006) was used as a secondary standard to estimate accuracy and precision. After trace element analyses, scanning electron microscopy (SEM) imaging was used to check for signal contamination (Fig. 1a and b). Signal stability was also carefully monitored for every analysis.

3. RESULTS AND DISCUSSION

3.1. Comparison between femtosecond LA-ICP-MS and SIMS

Our measurements on basalt standards BCR-2G and KL2-G (Fig. 2) provide a first order comparison of uncertainty and accuracy between the femtosecond LA-ICP-MS and Cameca IMS 3f series. Because a LA-ICP-MS measurement takes less than 3 min, we have managed to analyze several basalt standards throughout the course of the analytical session. On the contrary, the total analytical duration for a SIMS measurement over 17 elements takes

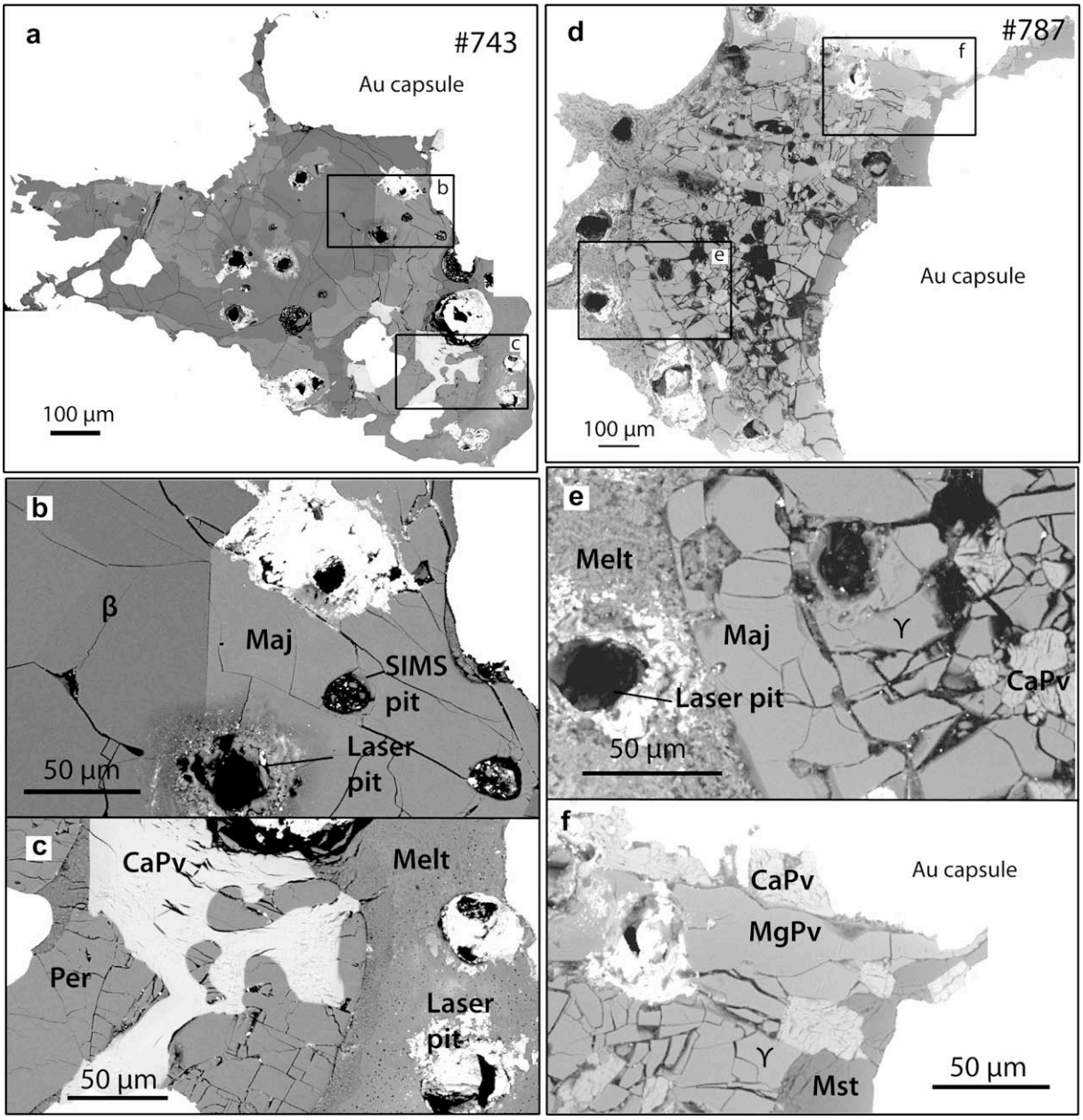

Fig. 1. Back-scattered electron images of run products. *Abbreviations used:* Maj, majoritic garnet; β, wadsleyite; γ, ringwoodite; CaPv, $CaSiO_3$ perovskite; MgPv, $MgSiO_3$ perovskite; Per, periclase; Mst, magnesite; Melt, quenched carbonate melt. (a) Overview of the experimental charges (#743; d, #787). (b) SIMS craters in a well-crystallized majorite garnet are visible, while laser pit may slightly overlap with β. (c) The melt forms homogeneous quench (#743) and poikilitic CaPv is observed next to melt and gas bubbles (#743 on a) probably formed during the quench. The melt has dendritic quench texture, and CaPv is around 50 µm across. (d) Sample #787, majorite garnet, MgPv and ringwoodite can only be recognized by microprobe analysis, see (e) and (f). These pictures were taken after repolishing, which explains the irregular form of the laser ablation craters and the occurrence of particles inside the craters (both SIMS and LA-ICP-MS).

nearly one hour; therefore fewer basalt standards were measured during these sessions. Therefore, the uncertainty of BCR-2G measurements (LA-ICP-MS) is given by the 2 standard deviation of the distribution of 4 measurements. The uncertainty of KL2-G measurement by SIMS is approximately 20% relative for most of the elements. These conservative estimates are based on the counting statistics of a typical counting rate.

The analyses obtained by fs LA-ICP-MS measurements are accurate to within 10% (except to within 17% for U) when compared with recommended concentrations of BCR-2G (Fig. 2). The concentrations obtained agree with the recommended values of BCR-2G (Fig. 2). The two standard deviations are approximately less than 8% relative for heavy REE, Hf, U and Th, while less than 5% for the other elements.

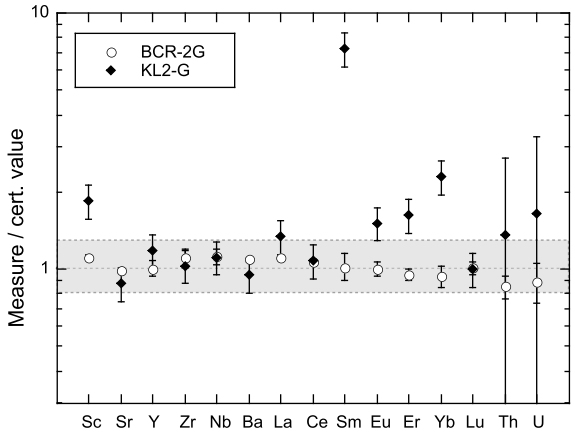

Fig. 2. Measurements of trace element compositions of known samples divided by the certified values. White circles are LA-ICP-MS data using BCR-2G, and black diamonds are SIMS data using KL2-G. Error bars are two standard deviations. The grey field represents ±20% relative deviation of standard values. Overall, LA-ICP-MS measurement show systematic variation within 20% of the standard value, while SIMS measurements could vary significantly more than ICP-MS measurements, suggesting severe matrix effects (e.g. oxide mass interferences). Especially, Sm shows an irreconcilable offset from the true value for SIMS analysis.

The accuracy of the SIMS results is less than previously reported values with the same instruments (5% relative for diopside PHN2661, Shimizu and Le Roex, 1986; with the IMS 3f at WHOI). Because of low counts, the offsets of Th and U are within the uncertainty based on the counting statistics (Fig. 2). This is most likely explained by the mass interferences since measurements of Sc, and mid to heavy REE (especially Sm, Eu) are notoriously prone to mass interferences. For example, there exists an interference with $^{29}Si^{16}O^{+}$ molecule at mass of $^{45}Sc^{+}$ (Steele et al., 1981; Weinbruch et al., 1993). We suspect that the offset of Sm is due to an interference with $^{135}Ba^{12}C$, and $^{134}Ba^{13}C$, since the samples had carbon coating prior to SIMS analyses, and is a carbonate-bearing experiment. Therefore, as we used the same isotopes for most of the element analyzed by LA-ICP-MS and SIMS, the offset of accuracy between LA-ICP-MS and SIMS is due to instrumental characteristics rather than the choice of mass peaks. This instrumental difference is, as a first order, the total count achieved by each technique, thus precision. The femtosecond LA-ICP-MS provides equivalent to more precise measurements than those of SIMS, due to its higher counting statistics. For instance, because of the higher counts, the femtosecond LA-ICP-MS is more suitable to measure U and Th in natural glasses than the SIMS. For SIMS, Th and U in KL2-G (1.0 and 0.55 ppm, respectively) give about 55 and 50 counts total, respectively. In contrast, for femtosecond LA-ICP-MS, these counts on BCR-2G (Th = 5.9 and U = 1.7 ppm) give about 1000 and 2300 counts total, respectively (total duration of analysis, approximately 2 min).

Despite these limitations, we presented all the SIMS measurements in this study since the partition coefficients by SIMS and LA-ICP-MS show a good agreement. The calculation of the partition coefficient appears to cancel out SIMS the molecular interferences that appear to be similar are identical for minerals and liquid.

3.2. Experimental products

We have conducted more than 10 experiments between 10 and 25 GPa, only two experiments (#743 obtained at 20 GPa 1600 °C during 23 h 30 min and #787 obtained at 25 GPa 1600 °C during 23 h) resulted in grain sizes and textures, that are suitable for trace element analyses. For sample #743, the experimental products consists of approximately 30% of majoritic garnet, 40% of wadsleyite, 25% of quenched carbonatitic melt and few percents of $CaSiO_3$ perovskite (CaPv) and periclase (Fig. 1a). Sample #787, consists of approximately 5% of majoritic garnet, 10% of Ca-Pv, 15% of $MgSiO_3$ perovskite (MgPv), 50% of ringwoodite, 10% of magnesite and 10% of quenched carbonate melt (Fig. 1b). Phase proportions reported here are calculated by mass-balance. Mineral assemblages of our samples are consistent with those obtained in peridotite compositions between 15 and 30 GPa (e.g. Zhang and Herzberg, 1994; Litasov and Ohtani, 2002). The nature of garnet (majoritic content: 51% for 743 sample and 31% for 787 sample) and the olivine polymorphs (wadsleyite and ringwoodite) were confirmed by Raman spectroscopy. Sample texture is appropriate for trace element analysis since grains are generally close to 50 μm in size (Fig. 1a and d). The liquid phase forms a separated volume situated at the edge of the capsule. In sample #743, periclase and CaPv are formed in proximity of melt. In sample #787, magnesite crystals are located opposite in the charge relative to the pooled melt. These textural observations suggest that a temperature gradient promoted phase segregation.

Major element compositions of each phase are presented in Table 1. The liquidus saturation of mantle phases was attained in both experiments. While the Mg-numbers (Mg/(Fe+Mg) molar) of the phases in sample #743 are consistent with those expected for mantle (e.g. wadsleyite = 0.92), the Mg-numbers of MgPv and ringwoodite in sample #778 are richer in Fe (0.87 and 0.85, respectively) due to the precipitation of magnesite. The lack of compositional zoning in crystals, indicates that a run duration of 23 h is sufficient to reach local chemical equilibrium. However, the mass-balance calculations using major elements failed to converge. Systematic excess or lack of oxides (CaO, MgO or Al_2O_3) from 20% to 30% was determined depending on the combination of oxides and phases. As inferred from the observed sample texture, the temperature gradient (<100 °C) is likely to have caused some disequilibrium at the scale of the entire sample. Nevertheless, CO_2 mass-balance succeeds with an excess of less than 2%. This suggests that CO_2 was equilibrated in the sample.

Trace element contents and corresponding partition coefficients ($D_i^{min/melt}$, wherein $D_i^{min/melt}$ is the concentration of element i in the mineral divided by concentration of the element i in the melt) for the phases in samples #743 (20 GPa, 1600 °C) and #787 (25 GPa, 1600 °C) are presented in Tables 2 and 3, respectively.

We have compared the sum of initial trace element masses with calculated sum based on the phase proportion of the charges. Nearly all elements converge within 40% deviation from the initial total. We admit that the recoveries of the calculated total trace element masses are poor, but this should be considered as reasonable results considering analytical uncertainty and poorly constrained mass-balance. The calculated total of all trace elements are in the same order of excess from the initial value, except for La in sample #743. Excess La could result from cell assembly contamination, although we did not identify excess of Cr or Zr.

Concentration differences between SIMS and LA-ICP-MS have little influence on calculated partition coefficients, in particular for rare earth element (REE) (Tables 2 and 3). However for Sc, Ba, Th and U, derived partition coefficients are significantly different. Because of significant difference in SiO_2 concentrations between carbonatitic melt and silicate minerals, it is possible that $^{29}Si^{16}O^{+}$ molecule causes the disparity in D_{Sc}. Nevertheless, even if this interference is corrected, the difference between ICP-MS values and SIMS values remains. Although we are unable to conclude which Sc partition coefficient is correct, we have used LA-ICP-MS Sc partition coefficients in the following discussion since they fit the elastic strain model better than those obtained by SIMS. Due the high incompatibility of Ba, the analyses in majoritic garnet were close to the detection limits of the LA-ICP-MS. The lower D_{Ba} obtained with the SIMS was chosen as the most representative. Because of better counting statistics, we prefer Th and U data from the LA-ICP-MS rather than SIMS. Our preferred partition coefficient values are noted *D* preferred in Tables 2 and 3 and are used in the following discussion.

3.3. Majoritic garnet–melt partitioning

Light rare earth elements (LREE), middle rare earth elements (MREE) and Sr, Zr, Hf, Ta, U and Th are incompatible in majoritic garnet whereas heavy rare earth elements (HREE), Sc and Y are compatible. The only previous studies on trace element partitioning between garnet and carbonatite melt are those from Sweeney et al. (1992) and Adam and Green (2001) which present partitioning data at pressures lower than 3 GPa, and that of Hammouda et al. (2008) at 7 GPa for Gd and Yb. There is a qualitative agreement on the compatible and incompatible nature of trace elements when we compare our data with data for low-pressure garnet (Sweeney et al., 1992; Adam and Green, 2001). A notable difference is that trace element partition coefficients are globally higher at 20 GPa, except for Zr, and HREE (Eu, Yb and Lu), which are less compatible than at lower pressure. These differences are likely related to variations of pressure and temperature conditions, and garnet major element composition (Adam and Green,

Table 3
Trace element concentrations (in ppm) of run product #787 (25 GPa, 1600 °C)

	Ca-Pv		Melt		$D^{\text{Ca-Pv/Melt}}$		
	LA-ICP-MS [2]	SIMS [1]	LA-ICP-MS [3]	SIMS [1]	LA-ICP-MS	SIMS	Preferred[c]
Sc	97(3)	156(3)	64(2)	101(4)	1.53(10)	1.54(9)	1.54(10)
Rb	n.m.	211(15)	n.m.	864(84)	—	0.24(4)	0.24(4)
Sr	427(2)	269(7)	726(15)	902(10)	0.588(14)	0.30(1)	0.40(1)
Y	817(23)	1099(27)	12.8(3)	19(1)	64(6)	58(4)	60(6)
Zr	831(30)	1010(30)	199(11)	246(17)	4.18(37)	4.11(41)	4.15(41)
Nb	254(11)	121(6)	561(38)	1092(26)	0.45(5)	0.111(8)	0.12(5)
Ba	658(24)	81(6)	1854(30)	2545(33)	0.35(2)	0.032(3)	0.032(3)*
Lc[b]	677(10)	*830(14)*	*104(3)*	132(2)	*6.5(3)*	6.3(2)	6.4(3)
Ce	896(7)	1018(15)	21.1(3)	21.5(6)	42.5(9)	47.4(20)	43.4(20)
Nd	n.m.	1191(21)	n.m.	22.1(7)	—	54(3)	54(3)
Sm	788(9)	1075(40)	11.2(2)	14.9(7)	70.4(18)	72(6)	71(6)
Eu	800(9)	1254(23)	10.9(2)	19.7(4)	73.5(18)	64(3)	70(18)
Gd	759(20)	1076(33)	10.3(3)	12.7(5)	73.6(41)	85(6)	77(6)
Tb	n.m.	1030(13)	n.m.	10.7(2)	—	96(4)	96(4)
Dy	n.m.	1143(29)	n.m.	12.5(5)	—	91(6)	91(6)
Ho	750(21)	1024(16)	10.7(3)	11.6(2)	69.9(41)	89(3)	81(3)
Er	761(25)	1013(22)	12.7(3)	13.5(4)	59.8(33)	75(5)	67(6)
Yb	734(17)	986(36)	18.8(5)	19.2(8)	39.1(19)	51(4)	41(4)
Lu	750(25)	945(16)	24.1(9)	22.3(3)	31.1(21)	42(1)	39(2)
Hf	373(10)	501(28)	226(4)	154(2)	1.65(7)	3.3(2)	1.8(2)
Ta	223(8)	n.m.	467(4)	n.m.	0.48(2)	—	0.48(2)
Th	1209(40)	1460(43)	11.4(4)	8.2(10)	106(8)	178(26)	112(26)
U	1036(48)	917(29)	7.3(4)	3.5(2)	141(14)	261(26)	168(26)

Number in parentheses represents two standards deviations in terms of least units cited. n.m.: not measured.
[a] Numbers in square brackets are numbers of LA-ICP-MS and SIMS analyse.
[b] La concentration in melt and mass-balance are suspect (see text). La contents are presented because they are consistent with other data (see below).
[c] Preferred *D* are weighted mean calculated from *D* determined by LA-ICP-MS and SIMS, except for * notation, *D* are chosen for reasons justified in the text.

2001; van Westrenen et al., 2001a; e.g. Draper et al., 2003; Draper and van Westrenen, 2007; van Westrenen and Draper, 2007).

Fig. 3a compares our *D*-values with those for majoritic garnet–silicate melt, from this study with *D*s obtained at 23–25 GPa, 2300 °C in CO_2-free mantle compositions (Corgne and Wood, 2004; Walter et al., 2004). Even though partitioning patterns look globally alike, differences in partitioning values between the two systems are significant. Sc and Y are more compatible in the carbonate system, while HREE, which are moderately incompatible in the CO_2-free silicate systems, are compatible in the carbonate system. Tetravalent HFSE (Zr, Hf) and MREE are less incompatible in the carbonate system with D_{Hf} is approach-

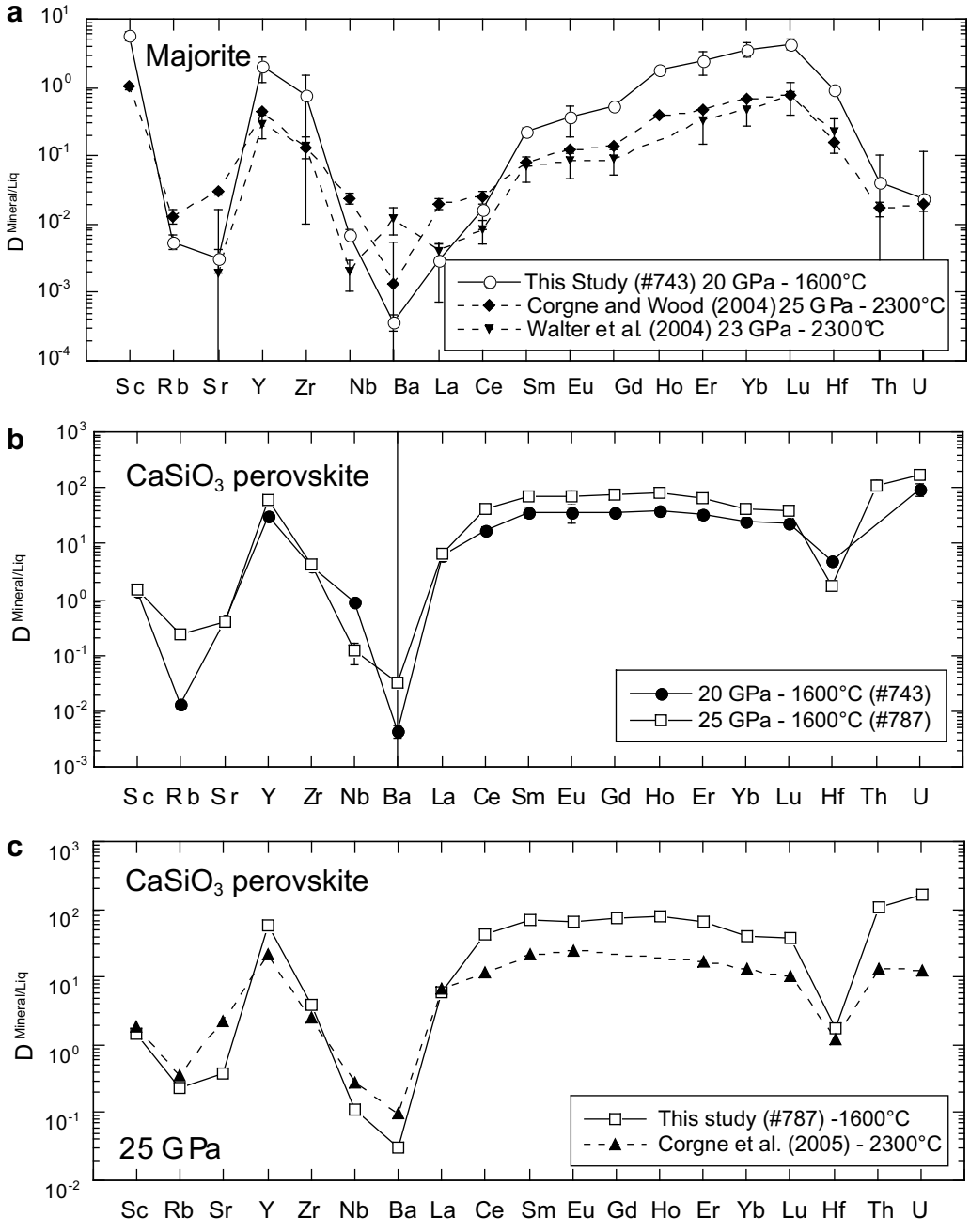

Fig. 3. Crystal-melt partitioning values for (a) Majorite garnet in comparison with Walter et al. (2004) and Corgne and Wood (2004) experimental data on majorite garnet–silicate melt partitioning at 23 and 25 GPa, respectively; (b) $CaSiO_3$ perovskite at 20 and 25 GPa. (c) Comparison of CaPv partitioning obtained in this study with Corgne et al. (2005) experimental data on $CaSiO_3$ perovskite at 25 GPa. Note that for REE $D^{Mineral/Carbonatitic\ melt}$ are 5 to 10 times higher than $D^{Mineral/Silicate\ melt}$. Temperature and melt composition appear to be the major factor controlling trace element partitioning. Elements are ordered with increasing atomic number.

ing 1.0. On the other hand, highly incompatible elements such as Sr, Nb, and La are more incompatible in the carbonate system. As shown in Fig. 3a, trace element patterns are more fractionated between majoritic garnet and carbonatitic melt than between majoritic garnet and silicate melt.

3.4. $CaSiO_3$ perovskite-melt partitioning

In agreement with the literature data, we found that REE, Y, Zr, Th and U are clearly compatible and Rb, Sr, Nb and Ba are incompatible, in CaPv at 20 and 25 GPa. Fig. 3b shows that the two patterns are similar, except for the most incompatible elements Rb, Nb and Ba. Rb and Ba are more incompatible at lower pressure while Nb is more compatible. Globally, Fig. 3b shows that between 20 and 25 GPa pressure has a minor effect on CaPv-melt partitioning of trace element. This result is consistent with the results from Corgne et al. (2005) who found that the combined effects of P and T between 20 GPa-2100 °C and 25 GPa-2300 °C are insignificant (their Fig. 2b).

Fig. 3c compares *D*-values from this study at 25 GPa with *D*-values obtained in a CO_2-free peridotite composition (25 GPa, 2300 °C; Corgne et al., 2005). Both CaPv were synthesized at the same pressure (25 GPa), therefore we can isolate the effects of temperature and composition on trace element partitioning. Although patterns are alike, notable differences are observed between the CO_2-bearing and CO_2-free systems. First Zr, Y, REE and Th and U are more compatible in CaPv in our 25 GPa experiment, and Sr and Ba are more incompatible. As previously noted for majoritic garnet, trace elements are more fractionated in carbonate systems than in CO_2-free silicate systems. The difference in *D*-values between both studies can be attributed to different temperature conditions (700 °C of difference between Corgne et al. (2005), and our study) and to differences in major element compositions: either crystal or melt major element composition. We note that there exist differences of major element compositions of majoritic garnet and of CaPv between our study and studies conducted in CO_2-free silicate systems (Corgne and Wood, 2004; Walter et al., 2004; Corgne et al., 2005). The majorite in the present study is less magnesian and three times more calcic than the majorite in CO_2-free silicate systems (Corgne and Wood, 2004; Walter et al., 2004). Similarly for CaPv at the same pressure of 25 GPa: CaPv in the CO_2-bearing system has less than 0.1% of MgO while in the CO_2-free silicate system CaPv is less calcic and contains more than 3% MgO.

3.5. Lattice strain models and their relations to crystal chemistry

*3.5.1. Regression of **D** to the lattice strain model*

Elemental partitioning between solid and liquid is partly controlled by crystal chemistry (e.g. Blundy and Wood, 1994, see also review by Blundy and Wood, 2003). Elements are incorporated in different crystal sites according to their ionic radius and charge. Each site is characterized by the parameters of the lattice strain model (Brice, 1975; Blundy and Wood, 1994). According to this model, for an isovalent-ion series of valence $n+$ and of radius r_i, which enters into a given crystal lattice site M, the partition coefficient (D_i) is described by three parameters: $r^{n+}_{0(M)}$, the ideal crystal site radius; E^{n+}_M, the elastic response of the site to the elastic strain caused by larger or smaller r_i than $r^{n+}_{0(M)}$; and $D^{n+}_{0(M)}$, the fictive strainless partition coefficient for a cation of radius $r^{n+}_{0(M)}$.

$$D_i = D^{n+}_{0(M)} \times \exp\left\{\frac{-4\pi N_A E^{n+}_M\left[\frac{1}{2}r^{n+}_{0(M)}(r_i - r^{n+}_{0(M)})^2 + \frac{1}{3}(r_i - r^{n+}_{0(M)})^3\right]}{RT}\right\}$$

where N_A is the Avogadro number, R is the gas constant and T is the temperature in K. Earlier studies focussed on low-pressure equilibria (see review by Blundy and Wood, 2003). However, this model is also applicable to high-pressure minerals like majoritic garnet and silicate perovskite (Corgne and Wood, 2002, 2004; Corgne et al., 2005).

Most majoritic garnets have a cubic symmetry (some have a tetragonal symmetry, Nakatsuka et al., 1999) with the general structural formula $X_3Y_2Z_3O_{12}$, where X-, Y- and Z-positions are dodecahedral, octahedral and tetrahedral cation sites, respectively (Heinemann et al., 1997). The presence of Si in both Y- and Z-sites is characteristic of a majorite component in the garnet. Accordingly, the increasing majorite component in garnet is characterized by: (1) increased Si (the Si excess, compared to pyrope garnet, is located in the Y-site), (2) presence of Fe and Mg in the Y-site, and lower Al. These variations are expressed by the substitution $^{VI}Si^{4+} + {}^{VI}[Ca + Mg + Fe] = 2^{VI}Al^{3+}$ (Draper et al., 2003). Here, we utilized a model wherein only Mg substitutes in the Y-site. Calcium and trivalent trace elements are assigned to the garnet X-site. $CaSiO_3$ perovskites has a cubic structure at lower mantle conditions (Kurashina et al., 2004; Ono et al., 2004) and contains two cation sites, an octahedral Si-site (6-fold coordination) and a dodecahedral Ca-site (12-fold coordination).

Because all trace elements investigated in this study have cation radii greater than r_{Mg}, they were allocated to the X-site of majoritic garnet and to the dodecahedral site of silicate perovskite. In principle, Sc^{3+}, Zr^{4+} and Hf^{4+} could enter in the X-site or Y-site of majoritic garnet and the dodecahedral or octahedral site of $CaSiO_3$ perovskites (Corgne and Wood, 2004; Corgne et al., 2005). As we succeed to fit these cation partition coefficients with partition coefficients of other isovalent cations on single lattice strain parabolas, we conclude that Sc^{3+}, Zr^{4+} and Hf^{4+} are predominantly substituted in the X-site in majoritic garnet and in the dodecahedral site in $CaSiO_3$ perovskites.

Fig. 4 shows that our data are accurately modeled using the lattice strain theory for most elements. This observation underlines the crystal structure contribution to majoritic garnet–carbonatitic melt partitioning and to $CaSiO_3$ perovskite–carbonatitic melt partitioning. Best-fit parameters of the lattice strain model r_0, D_0 and E are presented in Table 4, for divalent, trivalent and tetravalent cations, in 8-fold coordination for majorite and 12-fold coordination for $CaSiO_3$ perovskites.

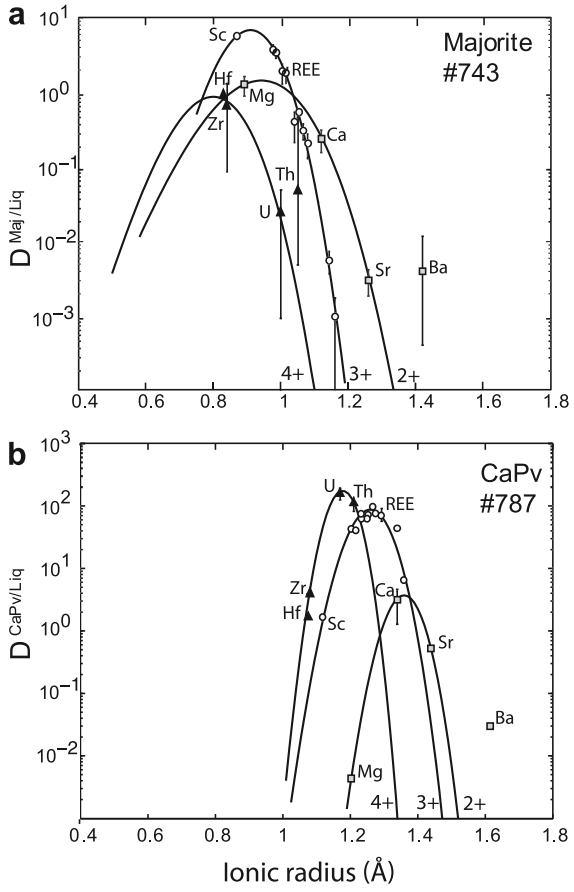

Fig. 4. Lattice strain models (Brice, 1975; Blundy and Wood, 1994) applied to crystal–carbonatite melt partition coefficients for (a) Majorite from run #743 and (b) $CaSiO_3$ perovskite from run #787. Note that, E increases with the increasing charge (width of parabolae). The position of the parabolae indicates that r_0 decreases with the increasing charge. Fit parameters obtained are listed in Table 4. Ionic radii are from taken Shannon (1976) and ionic radii for elements in 12-fold coordination have been linearly extrapolated with respect to coordination number. Despite the fact that Ca and Mg are not expected to behave like trace elements following Henri's law, 2+ cations lattice strain models are determined with Ca and Mg partition coefficient following Blundy and Wood (1994).

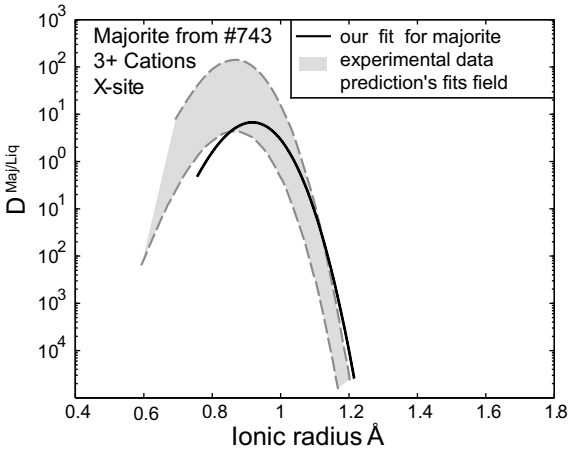

Fig. 5. The results of lattice strain modelling of partitioning of trivalent cations between the X-site of majorite garnet and carbonatite melt the experimental data of this study compared to the predictive garnet models from van Westrenen and Draper (2007) and Draper and van Westrenen (2007). The upper boundary is calculated using the thermodynamical prediction (van Westrenen and Draper, 2007) and the lower one is calculated employing the statistical prediction (Draper and van Westrenen, 2007). The parameters determined from the prediction models are presented in Table 4.

Measured D_{Ba} values, for both majorite and calcium silicate perovskites, are orders of magnitude too high to fit the divalent parabola. Consequently, D_{Ba} was excluded from the calculation for 2+ cations. Walter et al. (2004) previously noted that D_{Ba} is too large relative to lattice strain models in several minerals. Given that Ba^{2+} has the same ionic radius as O^{2-}, a substitution, $Ba^{2+} \leftrightarrow O^{2-} + Si^{4+}$, may occur in silicate minerals (e.g. Walter et al., 2004). This substitution would increase the compatibility of Ba in majoritic garnet and in $CaSiO_3$ perovskite.

3.5.2. Comparisons with predictive models of van Westrenen and Draper (2007) and Draper and van Westrenen (2007)

We compared our experimental data and measured parameters r_0, D_0 and for 3+ cations in the X-site of garnet with those calculated by the predictive model of Draper and van Westrenen (2007) and van Westrenen and Draper (2007), in Fig. 5 and Table 4. The value of E was successfully predicted using the model of van Westrenen and Draper (2007). The predicted r_0 is significantly lower than the r_0 modeled from our data, but within the reported uncertainty of 0.017 Å (1σ, van Westrenen and Draper, 2007). The difference can be explained by the fact that van Westrenen and Draper (2007) did not use majoritic components in their equation for r_0. We suggest that excess of Si entering in the garnet Y-site exerts an effect on r_0 of the X-site. We modeled D_0 with the statistical and the thermodynamic expression (Draper and van Westrenen, 2007; van Westrenen and Draper, 2007, respectively). Statistical prediction of D_0 appears to be closer to experimental value. The thermodynamic D_0 is especially affected by the Fe partition coefficient because it varies with melt composition and structure. Therefore, the thermodynamic D_0 is less likely to be applicable to carbonatitic melt system than the statistical D_0. Furthermore, activity model for REE species in van Westrenen and Draper's (2007) model assumes that dissolved species of REE in the melt conform with garnet stoichiometry. This assumption is highly unlikely in the case of carbonatitic melts, where the structure is dominated by carbonate anions (Treinman, 1989; Genge et al., 1994).

3.5.3. Majoritic garnet: comparison of carbonate and CO_2-free silicate systems

Comparison between lattice strain model fits for 2+, 3+ and 4+ cations for majoritic garnet in CO_2-free silicate systems (Corgne and Wood, 2004; noted with "silic" superscript hereafter) and in carbonate systems (noted with "carb" superscript hereafter) are presented in Fig. 6a. We

Table 4
Best-fit parameters for lattice strain model

Run	Charge	E (GPa)	r_0 (Å)	D_0
#743	*Majorite garnet*			
	2+	215(2)	0.940(1)	1.46(3)
	3+	522(3)	0.910(6)	6.9(13)
	4+	416(120)	0.80(26)	0.924(1)
#743	*$CaSiO_3$ perovskite*			
	2+	529(1)	1.355(4)	1.5(4)
	3+	585(0.7)	1.260(1)	41(4)
	4+	994(448)	1.18(50)	105(2)
#787	2+	900(5)	1.360(8)	3.6(61)
	3+	729(3)	1.260(5)	82(30)
	4+	1510(72)	1.175(5)	156(8)
	Majorite parameters from Corgne and Wood (2004)			
	2+	261	0.987	1.62
	3+	521(24)	0.908(3)	1.14(4)
	4+	522(327)	0.856(35)	0.15(3)
	Recalculated CaPv parameters (25 GPa) with 12-fold coordination from Corgne et al. (2005)			
	2+	258	1.35	5(1)
	3+	373(2)	1.270(7)	21(1)
	4+	459(42)	1.18(10)	11(1)
	Predicted parameters for majorite garnet from #743			
Model (20 GPa and 1600 °C)	3+	524	0.869	135.296[a] 4.405[b]

Number in parentheses represents one standard deviation in terms of least units cited.
Fitting was made for 2+ cations: Mg, Ca, Sr; for 3+ cations: Sc and REE; for 4+ cations: Hf, Zr and U (and Th for CaPv of #787).
[a] Thermodynamical prediction, van Westrenen and Draper (2007).
[b] Statistical prediction, Draper and van Westrenen (2007).

found that E^{4+} and r_0 for 4+ cations in the carbonate system are significantly lower than in the CO_2-free silicate systems while D_0 is higher (Table 4, Corgne and Wood, 2004). The ${r_0}^{3+}$ does not vary significantly between the two systems, but E^{3+} and ${D_0}^{3+}$ are higher in the carbonated system (Fig. 6a). Concerning 2+ cations, r_0 is higher in the carbonated system while E and notably, D_0 for divalent cations are essentially the same in the two systems. We find: ${}^{\text{carb}}{r_0}^{4+} < {}^{\text{silic}}{r_0}^{4+}$, ${}^{\text{carb}}{r_0}^{3+} \sim {}^{\text{silic}}{r_0}^{3+}$ and ${}^{\text{carb}}{r_0}^{2+} < {}^{\text{silic}}{r_0}^{2+}$; ${}^{\text{carb}}E^{4+} < {}^{\text{silic}}E^{4+}$, ${}^{\text{carb}}E^{3+} \sim {}^{\text{silic}}E^{3+}$ and ${}^{\text{carb}}E^{2+} < {}^{\text{silic}}E^{2+}$; and ${}^{\text{carb}}{D_0}^{4+} > {}^{\text{silic}}{D_0}^{4+}$, ${}^{\text{carb}}{D_0}^{3+} > {}^{\text{silic}}{D_0}^{3+}$ and ${}^{\text{carb}}{D_0}^{2+} < {}^{\text{silic}}{D_0}^{2+}$. As previously highlighted (e.g. van Westrenen et al., 2000; Corgne and Wood, 2004; Corgne et al., 2005), we found that r_0 decreases with increasing charge (Table 4). We expected $E^{2+} < E^{3+} < E^{4+}$ (Blundy and Wood, 1994, theoretically predicted that $E^{3+} = 1.5\ E^{2+}$ and $E^{4+} = 2\ E^{2+}$). However, in our lattice strain models, E does not vary linearly with charge because our E^{4+} is too low. We should mention that the uncertainty on E^{4+} is relatively large due to the large uncertainty on D_U.

According to van Westrenen and Draper (2007), r_0, E and D_0 depend on pressure, temperature and composition. The r_0 decreases with pressure and increases with temperature, while E and D_0 increase with pressure and decrease with temperature. Our majorite experiment is conducted at 5 GPa lower and 700 °C lower temperature than that of Corgne and Wood (2004). If the pressure is the dominant factor, the resulting relationship should be ${}^{\text{carb}}r_0 > {}^{\text{silic}}r_0$, ${}^{\text{carb}}E < {}^{\text{silic}}E$ and ${}^{\text{carb}}D_0 < {}^{\text{silic}}D_0$. On the contrary, if the temperature is the dominant factor, it should be ${}^{\text{carb}}r_0 < {}^{\text{silic}}r_0$, ${}^{\text{carb}}E > {}^{\text{silic}}E$ and ${}^{\text{carb}}D_0 > {}^{\text{silic}}D_0$. Table 4 shows that 2+ and 4+ data are consistent with temperature influence, whereas 3+ are ${}^{\text{carb}}r_0 \sim {}^{\text{silic}}r_0$ and ${}^{\text{carb}}E \sim {}^{\text{silic}}E$. Furthermore, Blundy and Dalton (2000) show for clinopyroxene-melt partitioning at 3 GPa and between 1375 and 1640 °C that r_0 and E values for the silicate system, at the same pressure and temperature conditions, are significantly different from those of carbonate system.

CaO content of majoritic garnet should have an influence on r_0 and E. Since Ca^{2+} is the major cation in the X-site, r_0 is expected to increase with Ca content (van Westrenen et al., 2001b). Comparing the major element composition of majoritic garnets, we note that our garnet has a Ca content 3 times higher than majoritic garnet in silicate system. Nevertheless, our current data cannot independently quantify the influence of CaO content on element partitioning excluding the pressure and temperature effect. Furthermore, van Westrenen and Draper (2007) predict that an increase in Ca garnet content should lower D_0, while all of our D_0 values are higher than those of Corgne and Wood (2004). We consider that our lower run temperature, which causes the increase of D_0 (van Westrenen and Draper, 2007), compensates the increase of Ca influence in garnet. To conclude, temperature has a major influence on the differences in lattice strain parameters between Corgne and Wood's (2004) study and our study, but is not sufficient to explain the ${r_0}^{3+}$ and E^{3+} data. We suggest that high Ca content of our garnet might also have an effect on r_0 and E.

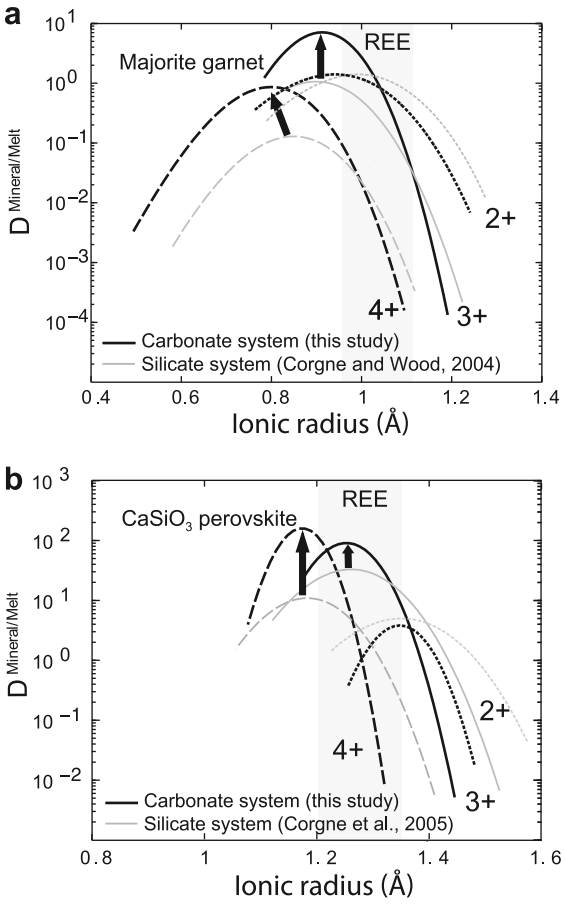

Fig. 6. Lattice strain model fits obtained for this study (solid black lines), compared with those obtained for the same minerals in silicate systems (solid gray lines, Corgne and Wood (2004) and Corgne et al. (2005) experimental data fits). Note that for all D-values of majorite garnet (3+, 4+) and CaPv (3+, 4+), carbonatitic system reveal higher D-values than silicate system, except for the larger ionic radii.

Lastly, we note that on top of these interpretations, the structure of the liquid can play a significant role in determining the value of D_0. According to Wood and Blundy (2001), the electrostatic work involved in the substitution ($\Delta G_{elec} = W_{elec}^{crystal} - W_{elec}$ where ΔG_{elec} is the free energy of substitution, W_{elec} refers to the electrostatic work done by either the crystal or the liquid in placing an ion in the crystal and in the liquid) varies according to the square of the charge difference between the tracer and the main site atom ($W = \frac{N_A(Z_c - Z_0)^2 e_0}{2\varepsilon r}$ where N_A is the Avogadro's number, $Z_c - Z_0$ is the effective radius of the defect of charge, e_0 is the charge of the electron, ε is the dielectric constant, r is the substituted ion radius). Furthermore, it concludes that the melt contribution to the electrostatic work is small compared to that of the crystal, because of the high disorder state of the melt and the presence of charge balancing cations. Because larger charge difference requires more electrostatic work for the substitution, the following relationship is generally inferred: $D_0^{2+} > D_0^{3+} > D_0^{4+}$. We, however, found that $D_0^{3+} > D_0^{2+} > D_0^{4+}$, while the majorite–$CO_2$-free silicate melt system resulted in $D_0^{2+} > D_0^{3+} > D_0^{4+}$. This suggests that there are non negligible electrostatic effects in the melt. Carbonatitic melts are based on $(CO_3)^{2-}$ anions with no tendency for polymerization (Treinman, 1989) and highly charged cation are not favored within such environment. Consequently, D_0^{3+} is greater than of D_0^{2+} while D_0^{4+} approaches D_0^{2+} (Fig. 6a). As another example, some clinopyroxene–carbonatite partitioning experiments (Blundy and Dalton, 2000) show $D_0^{3+} > D_0^{2+}$, while the clinopyroxene–silicate melt experiments result in $D_0^{2+} > D_0^{3+}$ (Wood and Blundy, 2001). However, at lower pressure, the order of D_0 always follows $D_0^{3+} > D_0^{2+}$ for the garnet–silicate melt system (see Draper and van Westrenen, 2007, for the data source). We propose here that the anomalous order of D_0 on partitioning in the majorite–carbonatite system is best explained by the influence of the melt structure above 20 GPa; however we cannot offer an explanation for the ubiquitous $D_0^{3+} > D_0^{2+}$ relationship for the low-pressure garnet–silicate melt system.

3.5.4. $CaSiO_3$ perovskite: comparison of carbonate and CO_2-free silicate systems

We found that r_0 decreases and D_0 increases with increasing charge. Comparing our data at 20 and 25 GPa, we found that there is no variation of r_0 with pressure, in contrast to E, which increases with increasing pressure. D_0^{2+} and D_0^{3+} are increased by a factor of 2 and D_0^{4+} is increased by ~30% when pressure is raised from 20 to 25 GPa. Theses variations could be due to a pressure effect or a variation of composition of the CaPv between 20 and 25 GPa. Available data do not allow discriminating between the two possibilities. Furthermore, we noted that CaPv at 20 GPa contains 10.5 wt% of trace elements, implying that Henry's law is surely violated. Corgne and Wood (2005) for example show that $D_{Th}^{CaPv/CO_2-freemelt}$ reduces for high Th abundance in CaPv.

Fig. 6b shows a comparison between the CaPv data in the carbonated system (this study) and those of Corgne et al. (2005) in CO_2-free silicate systems. Note that Corgne et al. (2005) used r_i for an 8-fold coordinated site, and here we recalculated their model fits with r_i values for 12-fold coordinated site by using to a linear extrapolation of relation between coordination and ionic radii values tabulated by Shannon (1976). We note that values of r_0 are similar in the two systems. E values are higher in the carbonate system than in CO_2-free silicate systems, which is most likely due to higher temperature in the study of Corgne et al. (2005). We infer that the temperature affects similarly on CaPv E parameter as in the case of majoritic garnet. As temperature increases, the X-site expands, thus E (or the Young modulus of the crystal) decreases. In both cases, r_o decreases with ionic charge increase whereas E increases, in agreement with lattice strain modeling (e.g. Wood and Blundy, 1997). A major feature of Fig. 6b is that values of D_0 are markedly higher in a carbonate system than in CO_2-free silicate systems. In a manner similar to the majorite case, the difference in D_o values can be addressed in terms of temperature and melt structure. We previously concluded that temperature increases D_0 values, but some

melt influence is noteworthy. We note that ${}^{carb}D_0{}^{2+} \sim {}^{silic}D_0{}^{2+}$, whereas ${}^{carb}D_0{}^{3+} > {}^{silic}D_0{}^{3+}$ and ${}^{carb}D_0{}^{4+} > {}^{silic}D_0{}^{4+}$. We found also that $D_0{}^{4+} > D_0{}^{3+} > D_0{}^{2+}$. Both studies conform that D_0-values for 3+ and 4+ are higher than $D_0{}^{2+}$. Although substitution mechanisms in perovskite appear to be rather complex and might involve Ca vacancies (Corgne and Wood, 2005) we cannot exclude that the change in the relative order of the parabolas in Fig. 6b can be attributed to an effect of the melt structure. On the basis of the electrostatic argument discussed above for majoritic garnet, we also suggest that, for perovskite–carbonate liquid partitioning, the melt structure has a measurable influence.

3.6. Implications for high-pressure carbonatitic melt metasomatism

Our liquidus saturation experiment suggests that a dolomite-bearing pyrolite composition can achieve an equilibrium between carbonatitic melt and transition zone mantle along the geotherm (our run condition 20 GPa, 1600 °C; also extrapolation from Dalton and Presnall, 1998). Furthermore, an experimental study showed that Na-rich pyroxene–enstatite inclusions in diamonds (Wang and Sueno, 1996) originate from lower mantle and/or transition zone conditions, and that the result from mantle metasomatism by a Na-rich carbonate melts (Gasparik and Hutchison, 2000). Carbonatitic melt cannot only be generated at transition zone conditions but also at conditions of the uppermost lower mantle (1600 °C, Gasparik and Litvin, 2002). A recent experimental and geochemical study on silicate mineral inclusions in diamond suggests the presence of carbonatitic melt at transition zone depths (Walter et al., 2008). Note however, that extrapolation of the melting phase diagram of carbonate-bearing peridotite from Dasgupta and Hirschmann (2006) suggests that carbonated peridotite melting never occurs along the geotherm at transition zone depths. This offset of carbonated peridotite melting between Dasgupta and Hirschmann (2006) and the present study can potentially be explained by the presence of 1500 ppm of H_2O in our samples. That could have lowered the carbonated peridotite solidus. We admit that there is considerable uncertainty whether cabonatitic melt can coexist with transition zone mantle. In following discussion, based on the reasons listed above, we consider the case where carbonatitic melt exists at transition zone depths.

It was previously suggested that magnesiocarbonatites, the most primary carbonatites are generated at pressures higher than 3 GPa (Bailey, 1989; Dalton and Presnall, 1998). However, carbonatite maximum source depth is still undetermined and our experimental data can provide additional constrains. While carbon-bearing, occasionally diamond-forming, fluid likely exists at transition zone depths, the investigations of carbonatite generation using major element composition are often hindered

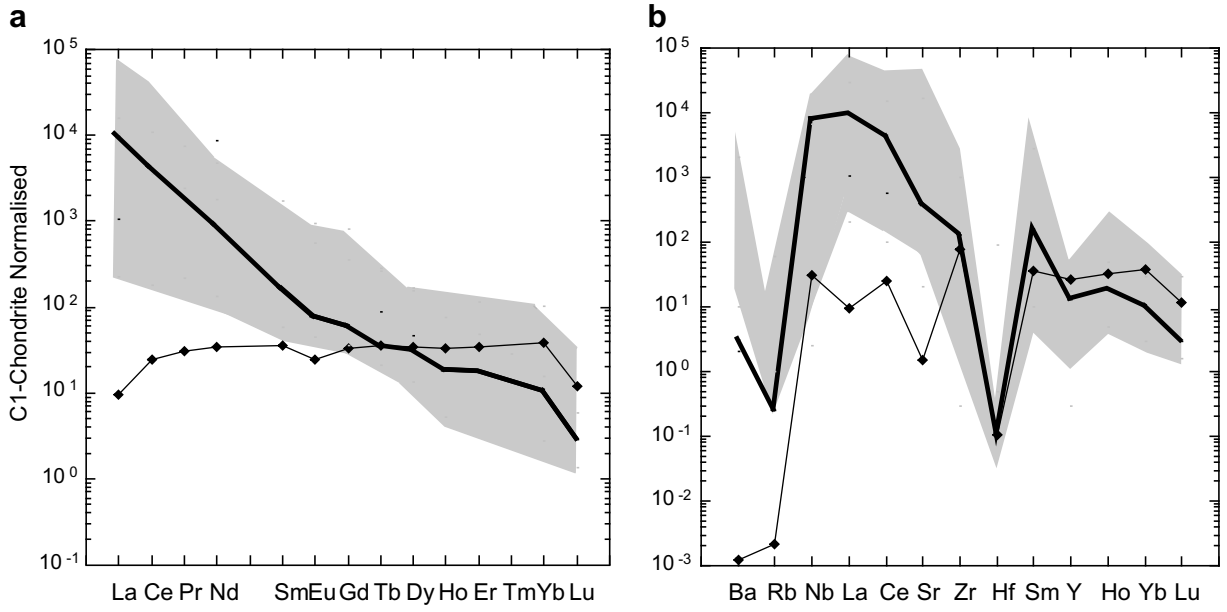

Fig. 7. Chondrite-normalised trace elements concentrations in natural magnesio- and calciocarbonatite compositions (data from von Maravic and Morteani, 1980; Gerlach et al., 1988; Nelson et al., 1988; Hornig-Kjarsgaard, 1998; Schultz et al., 2004) are shown as a grey area. Filled diamonds represent Kankan majorite inclusions in diamonds (Stachel et al., 2000). (a) REE patterns (b) patterns including other trace elements. Concentrations are normalized to Cl chondrite (McDonough and Sun, 1995). The bold lines represent the hypothetical melt compositions in equilibrium at 20 GPa with majoritic garnet composition (Stachel et al., 2000; majoritic garnets equilibrated at 13 GPa) with partition coefficients determined experimentally in this study. D_{Nd}, D_{Tb} and D_{Dy} have been calculated from our lattice strain modeling to limit the influence of analytical uncertainty on these data ($D_{Nd} = 0.04$, D_{Tb}=1.05 and $D_{Dy} = 1.08$). Note that the REE concentration of the carbonatitic melt in equilibrium at 20 GPa is in agreement with the high HREE concentration of the carbonatites. We stress that this deep carbonatitic melt also has the same relative element depletion and enrichment as carbonatites, except for Ba.

by crystallization and decarbonation reactions (e.g. Dalton and Presnall, 1998).

In contrast, trace element compositions are less prone to such limitation. Combining our partition coefficients for majorite–carbonatitic melt (run #743) with trace element compositions from majoritic garnets in inclusions in Kankan diamonds (Guinea, Stachel et al., 2000), we can estimate the trace element compositions of the carbonatitic melt that was potentially in equilibrium at 20 GPa and 1600 °C. Comparison with a range of REE patterns from natural carbonatites (von Maravic and Morteani, 1980; Gerlach et al., 1988; Nelson et al., 1988; Hornig-Kjarsgaard, 1998; Schultz et al., 2004) reveals that the transition zone carbonatitic melt REE pattern falls within the natural carbonatite field (Fig. 7a). Furthermore, the geochemical signature of deep carbonatitic melt is consistent with the flat HREE pattern of carbonatites. The geochemical signature of carbonatites is usually characterized by a depletion in Rb, Zr and Hf, and high Zr/Hf ratio (Hauri et al., 1993; Hoernle et al., 2002), and the Zr/Hf ratio of the deep carbonatitic melt is consistent with the carbonatites. However the model deep carbonatitic melt fails to reproduce the similar extent of the observed Ba enrichment relative to Rb (Fig. 7b). Perhaps, the appropriate value for D^{Ba} is much smaller than the one we have determined here. Alternatively, assuming that carbonatites are derived from deep carbonatitic metasomatism, some disparity of carbonatite geochemical signature (including for Ba) may be due to lower pressure reactions during the ascent of carbonatitic melt.

We have compared the trace element abundance of observed carbonatites at the surface and a carbonatitic melt equilibrated at 20 GPa. According to this model, carbonatitic melts must ascent to the surface, and preserve their trace element signature acquired at depth. Carbonatitic melts should interact with the surrounding mantle during ascent, but due to the highly enriched trace element abundance in carbonatitic melt, it is possible that the trace element signature is little affected by the interaction with olivine dominated mantle. The physical properties of carbonatitic melts may also reduce the potential interaction between melt and mantle. They have a low viscosity and density (Treinman, 1989; Genge et al., 1995; Dobson et al., 1996). They also form an interconnected network due to low wetting angle (Hunter and McKenzies, 1989; Watson, 1991), if there is no mixing with silicate melt (Minarik and Watson, 1995). They can quickly impregnate mantle rocks on a large scale by interfacial-driven infiltration (Hammouda and Laporte, 2000). Consequently, the residence time of carbonatitic melt in the mantle may be too short to result in a significant chemical exchange.

4. CONCLUSION

Here we report trace element partition coefficients measured between majoritic garnet and carbonatitic melt and between $CaSiO_3$ perovskite and carbonatitic melt. Trace element partition coefficients are more fractionated in carbonate system than in CO_2-free silicate systems, although similar patterns are obtained. Ba, Sr and LREE are more incompatible in carbonate systems while Sc, Y, HFSE, Zr and Hf, MREE and HREE are more compatible. Lattice strain models indicate that the difference of trace element partitioning between CO_2-free silicate melt and carbonatitic systems can mostly be attributed to different temperature conditions of respective experiments. Additionally, there are some potential influences by mineral and melt compositions.

Using partition coefficients determined in this study, we found that a carbonatitic melt potentially in equilibrium with majoritic garnet inclusions in diamonds has a geochemical signature similar to that of some natural carbonatite lavas. This suggests that carbonatitic metasomatism can exist in the transition zone.

ACKNOWLEDGMENTS

We really want to thank Jean-Luc Devidal (LMV) for microprobe analysis, Jean-Marc Henot for well-tuned back-scattered electron images, Remi Freydier and Frédéric Candaudap for their help with LA-ICP-MS analysis. Nobu Shimizu gave us access to WHOI 3f SIMS, and Bernard Boyer's assistance at GM 4f SIMS was insightful. Audrey Martin is also acknowledged for her help on multi-anvil apparatus and we gratefully thank Nathalie Bolfan-Casanova for her help on multi-anvil press calibrations and references. The manuscript was significantly improved by the thoughtful, and critical, comments of A. Corgne, W. Van Westrenen, P. Ulmer and an anonymous reviewer. The multianvil apparatus of Laboratoire Magmas et Volcans is financially supported by the Centre National de la Recherche Scientifique (Instrument National de l'INSU). Analyses were supported by CNRS funding to LMV, by a BQR to Kenneth T. Koga, and partly by the "ANR Jeunes Chercheurs" 2006 of Estelle F. Rose-Koga.

REFERENCES

Adam J. and Green T. (2001) Experimentally determined partition coefficients partition coefficients for minor and trace elements in peridotite minerals and carbonatite melt, and their relevance to natural carbonatites. *Eur. J. Mineral.* **13**, 815–827.

Akaogi M., Yusa H., Shiraishi K. and Suzuki T. (1995) Thermodynamic properties of alpha -quartz, coesite, and stishovite and equilibrium phase relations at high pressures and high temperatures. *J. Geophys. Res. B Solid Earth Planets* **100**(11), 22337–22347.

Bailey D. K. (1989) Carbonate melt from the mantle in the volcanoes of south-east Zambia. *Nature* **388**, 415–418.

Blundy J. and Dalton J. (2000) Experimental comparison of trace element partitioning between clinopyroxene and melt in carbonate and silicate systems, and implications for mantle metasomatism. *Contrib. Mineral. Petrol.* **139**, 356–371.

Blundy J. and Wood B. (1994) Prediction of crystal-melt partition coefficients from elastic moduli. *Nature (London)* **372**, 452–454.

Blundy J. and Wood B. (2003) Partitioning of trace elements between crystals and melts. *Earth Planet. Sci. Lett.* **210**(3–4), 383–397.

Brice J. C. (1975) Some thermodynamic aspects of the growth of strained crystals. *J. Crystal Growth* **28**, 249–253.

Coltice N., Simmon L. and Lecuyer C. (2004) Carbon isotope cycle and mantle structure. *Geophys. Res. Lett.* **31**, 1–5.

Corgne A. and Wood B. J. (2002) $CaSiO_3$ and $CaTiO_3$ perovskite-melt partitioning of trace elements: implications for gross mantle differentiation. *Geophys. Res. Lett.* **29**(19), 1933.

Corgne A. and Wood B. (2004) Trace element partitioning between majoritic garnet and silicate melt at 25 GPa: new developments in high-pressure mineral physics and applications to the Earth's interior. *Phys. Earth Planet. Interiors* **143**, 407–419.

Corgne A. and Wood B. (2005) Trace element partitioning and substitution mechanisms in calcium perovskites. *Contrib. Mineral. Petrol.* **149**, 85–97.

Corgne A., Liebske C., Wood B. J., Rubie D. C. and Frost D. J. (2005) Silicate perovskite-melt partitioning of trace elements and geochemical signature of a deep perovskitic reservoir. *Geochim. Cosmochim. Acta* **69**(2), 485–496.

Dalton J. A. and Presnall D. C. (1998) The continuum of primary carbonatitic–kimberlitic melt compositions in equilibrium with lherzolite: data from the system $CaO–MgO–Al_2O_3–SiO_2–CO_2$ at 6 GPa. *J. Petrol.* **39**(11–12), 1953–1964.

Dasgupta R., Hirschmann M. and Withers A. C. (2004) Deep global cycling of carbon constrained by the solidus of anhydrous, carbonated eclogite under upper mantle conditions. *Earth. Planet. Sci. Lett.* **227**, 73–85.

Dasgupta R. and Hirschmann M. M. (2006) Melting in the Earth's deep upper mantle caused by carbon dioxide. *Nature* **440**, 659–662.

Dobson D. P., Jones A. P., Rabe R., Sekine T., Kurita K., Taniguchi T., Kondo T., Kato T., Shimomura O. and Urakawa S. (1996) In-situ measurement of viscosity and density of carbonate melts at high pressure. *Earth Planet. Sci. Lett.* **143**(1–4), 207–215.

Draper D. S. and van Westrenen W. (2007) Quantifying garnet-melt trace element partitioning using lattice–strain theory: assessment of statistically significant controls and new predictive model. *Contrib. Mineral. Petrol.* **154**, 731–746.

Draper D. S., Xirouchakis D. and Agee C. B. (2003) Trace element partitioning between garnet and chondritic melt from 5 to 9 GPa: implications for the onset of the majorite transition in the Martian mantle. Diffusion and partitioning in planetary interiors. *Phys. Earth Planet. Interiors* **139**, 149–169.

Dupuis C., Liotard J. M. and Dostal J. (1992) Zr/Hf fractionation in intraplate basaltic rocks: carbonate metasomatism in mantle source. *Geochim. Cosmochim. Acta* **56**, 2417–2423.

Eggler D. H. (1976) Does CO_2 cause partial melting in the low-velocity layer of the mantle? *Geology* **4**, 69–72.

Freydier R., Candaudap F., Poitrasson F., Arbouet A., Dupre B. and Chatel B. (2008) Evaluation of infrared femtosecond laser ablation for the analysis of geomaterials by ICP-MS. *J. Anal. At. Spectrom.* **23**, 702–710.

Gasparik T. and Litvin Y. A. (2002) Experimental investigation of the effect of metasomatism by carbonatic melt on the composition and structure of the deep mantle. *Lithos* **60**(3–4), 129–143.

Gasparik T. and Hutchison M. T. (2000) Experimental evidence for the origin of two kinds of inclusions in diamonds from the deep mantle. *Earth Planet. Sci. Lett.* **181**(1–2), 103–114.

Genge M. J., Jones A. P. and Price G. D. (1994) An infrared and Raman study of carbonate glasses: implications for the structure of carbonatite magmas. *Geochim. Cosmochim. Acta* **59**(5), 927–937.

Genge M. J., Price G. D. and Jones A. P. (1995) Molecular dynamics simulations of $CaCO_3$ melts to mantle pressures and temperatures: implications for carbonatite magmas. *Earth Planet. Sci. Lett.* **131**, 225–238.

Gerlach D. C., Cliff R. A., Davies G. R., Norry M. and Hodgson N. (1988) Magma sources of the Cape Verdes Archipelago; isotopic and trace element constraints. *Geochim. Cosmochim. Acta* **52**(12), 2979–2992.

Green D. H. and Ringwood A. E. (1963) Mineral assemblages in a model mantle composition. *J. Geophys. Res.* **68**, 937–945.

Green D. H. and Wallace M. (1988) Mantle metasomatism by ephemeral carbonatite melts. *Nature* **336**(6198), 459–462.

Hammouda T. (2003) High-pressure melting of carbonated eclogite and experimental constraints on carbon recycling and storage in the mantle. *Earth Planet. Sci. Lett.* **214**, 357–368.

Hammouda T. and Laporte D. (2000) Ultrafast mantle impregnation by carbonatite melts. *Geology* **28**, 283–285.

Hammouda T., Moine B. N., Devidal J. L. and Vincent C. (2008) Trace element partitioning during partial melting of carbonated eclogites. *Physics of the Earth and Planetary Interiors*. doi:10.1016/j.pepi.2008.06.009.

Harte B., Harris J. W., Hutchison M. T., Watt G. R. and Wilding M. C. (1999) Lower mantle mineral associations in diamonds from Sao Luiz, Brazil. *Mantle petrology; field observations and high-pressure experimentation; a tribute to Francis R. (Joe) Boyd. Special Publication—Geochemical Society* **6**, 125–153.

Hauri E. H., Shimizu N., Dieu J. J. and Hart S. R. (1993) Evidence for hotspot-related carbonatite metasomatism in the oceanic upper mantle. *Nature (London)* **365**, 221–227.

Heinemann S., Sharp T. G., Seifert F. and Rubie D. C. (1997) The cubic-tetragonal phase transition in the system majorite $Mg_4Si_4O_{12}$-pyrope $Mg_3Al_2Si_3O_{12}$. *Phys. Chem. Miner.* **24**(3), 206–221.

Hoernle K., Tilton G., LeBas M. J. and Garbe-Schoenberg D. (2002) Geochemistry of oceanic carbonatites compared with continental carbonatites; mantle recycling of oceanic crustal carbonate. *Contrib. Mineral. Petrol.* **142**(5), 520–524.

Hornig-Kjarsgaard I. (1998) Rare earth elements in Sovitic carbonatites and their mineral phases. *J. Petrol.* **39**(11–12), 2105–2121.

Hunter R. H. and McKenzies D. (1989) The equilibrium geometry of carbonate melts in rocks of mantle composition. *Earth Planet. Sci. Lett.* **92**, 347–356.

Hutchison M. T., Hursthouse M. B. and Light M. E. (2001) Mineral inclusions in diamonds; associations and chemical distinctions around the 670-km discontinuity. *Contrib. Mineral. Petrol.* **142**, 119–126.

Irifune T., Kiozumi T. and Ando J.-i. (1996) An experimental study of the garnet-perovskite transformation in the system $MgSiO_3$-$Mg_3Al_2Si_3O_{12}$. *Physics of the Earth and Planetary Interiors* **96**, 147–157.

Ionov D. A. (2001) Carbonates in mantle xenoliths; quenched melts or crystal cumulates? *J. African Earth Sci.* **32**, A19.

Ionov D. A., Dupuy C., O-Reilly S. Y., Kopylova M. G. and Genshaft Y. S. (1993) Carbonate-bearing peridotite xenoliths from Spitsbergen; implications for trace element signature of mantle carbonate metasomatism. *Earth Planet. Sci. Lett.* **119**(3), 283–297.

Itie J. P., Polian A., Jauberthie-Carillon C., Dartyge E., Fontaine A., Tolentino H. and Tourillon G. (1989) High-pressure phase transition in gallium phosphide: an X-ray-absorption spectroscopy study. *Phys. Rev. B Condens. Matter* **40**(14), 9709–9714.

Javoy M. and Pineau F. (1991) The volatiles record of a "popping" rock from the Mid-Atlantic Ridge at 14°N: chemical and isotopic composition of gas trapped in the vesicles. *Earth Planet. Sci. Lett.* **107**(3–4), 598–611.

Jochum K. P. and Stoll B. (2006) MPI-DING reference glasses for in situ microanalysis: new reference values for element concentrations and isotope ratios. *Geochem. Geophys. Geosyst. G3* **7**, Q02008.

Jones A. P. (1989) Upper-mantle enrichment by kimberlitic or carbonatitic magmatism. In *Carbonatites: Genesis and Evolution* (ed. K. Bell). Unwin Hyman, London, pp. 48–461.

Katsura T. and Ito E. (1989) The system Mg_2SiO_4–Fe_2SiO_4 at high pressures and temperatures; precise determination of stabilities

of olivine, modified spinel, and spinel. *J. Geophys. Res. B Solid Earth Planets* **94**(11), 15663–15670.

Katsura T., Yamada H., Shinmei T., Kubo A., Ono S., Kanzaki M., Yoneda A., Walter M. J., Ito A., Urakawa S., Funakoshi K. and Utsumi W. (2003) Post-spinel transition in Mg_2SiO_2 determined by high P-T in situ X-ray diffractometry. *Phys. Earth Planet. Interiors* **136**, 11–24.

Kawai N. and Endo S. (1970) The generation of ultrahigh hydrostatic pressures by a split sphere apparatus. *Rev. Sci. Instrum.* **41**(8), 1178–1181.

Keller J. and Krafft M. (1990) Effusive natrocarbonatite activity of Oldoinyo Lengai, June. *Bull. Volcanol.* **52**(8), 629–645.

Keshav S., Corgne A., Gudfinnsson G. H., Bizimis M., McDonough W. F. and Fei Y. (2005) Kimberlite petrogenesis; insights from clinopyroxene-melt partitioning experiments at 6 GPa in the $CaO–MgO–Al_2O_3–SiO_2–CO_2$ system. *Geochim. Cosmochim. Acta* **69**, 2829–2845.

Klemme S., van der Laan S. R., Foley S. F. and Gunther D. (1995) Experimentally determined trace and minor element partitioning between clinopyroxene and carbonatite melt under upper mantle conditions. *Earth Planet. Sci. Lett.* **133**(439–448).

Krafft M. and Keller J. (1989) Temperature measurements in carbonatite lava lakes and flows from Oldoinyo Lengai, Tanzania. *Science* **245**, 168–170.

Kunz M., Gillet P., Fiquet G., Sautter V., Graafsma H., Conrad P. and Harris J. W. (2002) Combined in situ X-ray diffraction and Raman spectroscopy on majoritic garnet inclusions in diamonds. *Earth Planet. Sci. Lett.* **198**, 485–493.

Kurashina T., Hirose K., Ono S., Sata N. and Ohishi Y. (2004) Phase transition in Al-bearing $CaSiO_3$ perovskite; implications for seismic discontinuities in the lower mantle. *Phys. Earth Planet. Interiors* **145**(1–4), 67–74.

Litasov K. and Ohtani E. (2002) Phase relations and melt compositions in CMAS-pyrolite-H_2O system up to 25 GPa. *Phys. Earth Planet. Interiors* **134**(1–2), 105–127.

McDonough W. F. and Sun S.-s. (1995) The composition of the Earth. *Chem. Geol.* **120**, 223–253.

Mc Mahon M. I., Nelmes R. J., Allan D. R., Belmonte S. A. and Bovornrataraks T. (1998) Observation of a simple-cubic phase of GaAs with 16-atom basis (SC16). *Phys. Rev. Lett.* **80**(25), 5564–5567.

Meens J. K., Ayers J. C. and Fregeau E. J. (1989) A model of mantle metasomatism by carbonated alkali melts: trace-element and isotopic compositions of mantle source regions of carbonatite other continental igneous rocks. In *Carbonatites: Genesis and Evolution* (ed. K. Bell). Unwin Hyman, London, pp. 464–495.

Menzies M. A. and Wass S. Y. (1983) CO_2- and LREE-rich mantle below eastern Australia; a REE and isotopic study of alkaline magmas and apatite-rich mantle xenoliths from the Southern Highlands Province, Australia. *Earth Planet. Sci. Lett.* **65**, 287–302.

Minarik W. G. and Watson E. B. (1995) Interconnectivity of carbonate melt at low melt fraction. *Earth Planet. Sci. Lett.* **133**(3–4), 423–437.

Molina J. F. and Poli S. (2000) Carbonate stability and fluid composition in subducted oceanic crust; an experimental study on $H_2O–CO_2$-bearing basalts. *Earth Planet. Sci. Lett.* **176**, 295–310.

Morishima H., Kato T., Suto M., Ohtani E., Urakawa S., Utsumi W., Shimomura O. and Kikegawa T. (1994) The phase boundary between α and β Mg_2SiO_4 determined by in situ X-ray observation. *Science* **265**(5176), 1202–1203.

Nakatsuka A., Yoshiasa A., Yamanaka T., Ohtaka O., Katsura T. and Ito E. (1999) Symmetry change of majorite solid-solution in the system $Mg_3Al_2Si_3O_{12}–MgSiO_3$. *Am. Mineral.* **84**, 1135–1143.

Nelson D. R., Chivas A. R., Chappell B. W. and McCulloch M. T. (1988) Geochemical and isotopic systematics in carbonatites and implications for the evolution of ocean-island sources. *Geochim. Cosmochim. Acta* **52**, 1–17.

Ono S., Ohishi Y. and Mibe K. (2004) Phase transition of Ca-perovskite and stability of Al-bearing Mg-perovskite in the lower mantle. *Am. Mineral.* **89**(10), 1480–1485.

O'Reilly S. Y. and Griffin W. L. (1988) Mantle metasomatism beneath western Victoria, Australia: I. Metasomatic processes in Cr-diopside lherzolites. *Geochim. Cosmochim. Acta* **52**, 433–448.

Pan Y., Qu S., Dong S., Cui Q., Zhang W., Liu X., Liu J., Liu B., Gao C. and Zou G. (2002) An investigation on the pressure-induced phase transition of nanocrystalline ZnS. Special issue containing articles presented at the 18th International Conference of High Pressure Science and Technology and the 11th High Pressure Conference in China. *J. Phys. Condens. Matter* **14**(44), 10487–10490 (print).

Pearce N. J. G., Perkins W. T., Westgate J. A., Gorton M. P., Jackson S. E., Neal C. R. and Chenery S. P. (1997) A compilation of new and published major and trace element data for NIST SRM 610 and NIST SRM 612 glass reference materials. *Geostandard. Newslett.* **21**, 115–144.

Poitrasson F., Mao X., Mao S. S., Freydier R. and Russo R. E. (2003) Comparison of ultraviolet femtosecond and nanosecond laser ablation inductively coupled plasma mass spectrometry analysis in glass, monazite and zircon. *Anal. Chem.* **75**, 6184–6190.

Price S. E., Russell J. K. and Kopylova M. G. (2000) Primitive magma from Jericho pipe, N W.T., Canada: constraints on primary kimberlite melt chemistry. *J. Petrol.* **41**(6), 789–808.

Reed W. P. (1992) Certificate of analysis, standard reference materials 610 611. (National Institute of Standard and Technology).

Rudnick R. L., McDonough W. F. and Chappell B. W. (1993) Carbonatite metasomatism in the northern Tanzanian mantle; petrographic and geochemical characteristics. *Earth Planet. Sci. Lett.* **114**, 463–475.

Sarda P. and Guillot B. (2005) Breaking of Henry's law for noble gas and CO_2 solubility in silicate melt under pressure. *Nature (London)* **436**, 95–98.

Schultz F., Lehmann B., Tawackoli S., Roessling R., Belyatsky B. and Dulski P. (2004) Carbonatite diversity in the Central Andes; the Ayopaya alkaline province, Bolivia. *Contrib. Mineral. Petrol.* **148**, 391–408.

Shannon R. D. (1976) Revised effective ionic radii and systematic studies of iteratomic distances in halides and chalcogenides. *Acta Cryst.* **A32**, 751–767.

Shimizu N. and Hart S. R. (1982) Application of the ion microprobe to geochemistry and cosmochemistry. *Ann. Rev. Earth Planet. Sci.* **10**, 483–526.

Shimizu N. and Le Roex A. P. (1986) The chemical zoning of augite phenocrysts in alkaline basalts from Gough Island, South Atlantic. *J. Volcanol. Geotherm. Res.* **29**, 159–188.

Stachel T., Brey G. P. and Harris J. W. (2000) Kankan diamonds (Guinea) I: from the lithosphere down to the transition zone. *Contrib. Mineral. Petrol.* **140**, 1–15.

Steele I. M., Hervig R. L., Hutcheon I. D. and Smith J. V. (1981) Ion micro-probe techniques and analyses of olivine and low-Ca pyroxene. *Am. Mineral.* **66**(5–6), 526–546.

Sweeney R. J., Green D. H. and Sie S. H. (1992) Trace and minor element partitioning between garnet and amphibole and carbonatitic melt. *Earth Planet. Sci. Lett.* **113**(1–2), 1–14.

Treinman A. H. (1989) Carbonatite magma: properties and processes. In *Carbonatites: Genesis and Evolution* (ed. K. Bell). Unwin Hyman, London, pp. 89–104.

van Westrenen W., Allan N. L., Blundy J. D., Purton J. A. and Wood B. J. (2000) Atomistic simulation of trace element incorporation into garnets; comparison with experimental garnet-melt partitioning data. *Geochim. Cosmochim. Acta* **64**(9), 1629–1639.

van Westrenen W., Wood B. J. and Blundy J. D. (2001b) A predictive thermodynamic model of garnet-melt trace element partitioning. *Contrib. Mineral. Petrol.* **142**(2), 219–234.

van Westrenen W., Blundy J. D. and Wood B. J. (2001a) High field strength element/rare earth element fractionation during partial melting in the presence of garnet; implications for identification of mantle heterogeneities. *Geochem. Geophys. Geosyst.-G 3* **2**, Paper No. 2000GC000133.

van Westrenen W. and Draper D. S. (2007) Quantifying garnet-melt trace element partitioning using lattice–strain theory: new crystal-chemical and thermodynamic constraints. *Contrib. Mineral. Petrol.* **154**, 717–730.

von Maravic H. and Morteani G. (1980) Petrology and geochemistry of the carbonatite and syenite complex of Lueshe (N.E. Zaire). *Lithos* **13**(2), 159–170.

Walker D., Carpenter M. A. and Hitch C. M. (1990) Some simplifications to multianvil devices for high pressure experiments. *Am. Mineral.* **75**, 1020–1028.

Walter M. J., Bulanova G. P., Armstrong L. S., Keshav S., Blundy J. D., Gudfinnson G., Lord O. T., Lennie A. R., Clark S. M., Smith C. B. and Gobbo L. (2008) Primary carbonatite melt from deeply subducted oceanic crust. *Nature* **454**, 622–625.

Walter M. J., Nakamura E., Trønnes R. G. and Frost D. J. (2004) Experimental constraints on crystallization differentiation in a deep magma ocean. *Geochim. Cosmochim. Acta* **68**(20), 4267–4284.

Wang W. and Sueno S. (1996) Discovery of a NaPx-En inclusion in diamond: possible transition zone origin. *Mineral. J.* **18**, 9–16.

Watson E. B. (1991) Diffusion fluid-bearing and slightly-melted rocks-experimental and numerical approaches illustrated by iron transport in dunite. *Contrib. Mineral. Petrol.* **107**, 417–434.

Watson E. B., Brenan J. M. and Baker D. R. (1990) Distribution of fluids in the continental mantle; continental mantle. *Oxford Monogr. Geol. Geophys.* **16**(111–125).

Weinbruch S., Specht S. and Palme H. (1993) Determination of Fe, Mn, Ni and Sc in Olivine by secondary ion mass-spectrometry. *European Journal of Mineralogy* **5**(1), 37–41.

Wilson S. A. (1997) The collection, preparation, and testing of USGS reference material BCR-2, Columbia River, Basalt.

Wood B. J. and Blundy J. D. (1997) A predictive model for rare earth element partitioning between clinopyroxene and anhydrous silicate melt. *Contrib. Mineral. Petrol.* **129**(2–3), 166–181.

Wood B. J. and Blundy J. D. (2001) The effect of cation charge on crystal–melt partitioning of trace elements. *Earth Planet. Sci. Lett.* **188**(1–2), 59–71.

Wyllie P. J. and Huang W. L. (1975) Influence of mantle CO_2 in the generation of carbonatites and kimberlites. *Nature* **257**, 297–299.

Yaxley G. M., Crawford A. J. and Green D. H. (1991) Evidence for carbonatite metasomatism in spinel peridotite xenoliths from western Victoria, Australia. *Earth Planet. Sci. Lett.* **107**, 305–317.

Zhang Y. and Zindler A. (1993) Distribution and evolution of carbon and nitrogen in Earth. *Earth Planet. Sci. Lett.* **117**, 331–345.

Zhang J. and Herzberg C. (1994) Melting experiments on anhydrous peridotite KLB-1 from 5.0 to 22.5 GPa. *J. Geophys. Res. B Solid Earth Planets* **99**(9), 17729–17742.

Associate editor: Peter Ulmer